

NUMERICAL ANALYSIS OF THE TRAILING-EDGE VORTEX LAYER AND THE WAKE-VORTEX SYSTEM OF A GENERIC TRANSPORT-AIRCRAFT CONFIGURATION

S. Pfnür

Chair of Aerodynamics and Fluid Mechanics, Technical University of Munich
Boltzmannstr. 15, 85748 Garching, Germany

Abstract

The trailing-edge flow and wake-vortex system are numerically investigated on a generic transport-aircraft configuration, the Common Research Model (CRM). The analysis is performed for cruise condition with a Mach number of $Ma = 0.85$, a Reynolds number of $Re = 5 \cdot 10^6$ and an angle of attack of $\alpha = 2^\circ$. A time-accurate Reynolds-Averaged Navier-Stokes simulation applying the Menter-SST model is performed, which also allows for the representation of the starting vortex at the wing. The trailing-edge compatibility condition, derived with certain restrictions (e.g. $Re \rightarrow \infty$) is evaluated for the Common Research Model. The trailing-edge compatibility condition gives a relation between the flow velocity profiles in the vortex layer near the wing trailing edge and the bound circulation along the wing. Although effects at the wing are present for the investigated case, which are not considered by the trailing-edge compatibility condition, the circulation distribution along the wing is predicted very well. Furthermore, the wake-vortex system is investigated with focus on the circulation of the wake. The absolute value of the overall circulation in the wake and its conservation in downstream direction are appropriately predicted. The roll-up process of the vortex layer into the trailing vortex is depicted and the associated characteristics of an increase of the circulation in the trailing vortex during the roll-up stage is proven as well.

NOMENCLATURE

A_{ref}	Wing planform area, [m ²]	x^1, x^2, x^3	Local wake coordinates, [m]
b	Wing span, [m]	y^+	Dimensionless wall distance
c_L	Lift coefficient, $c_L = \frac{L}{q_\infty \cdot S_{Ref}}$	α	Angle of attack, [deg]
c_l	Lift coefficient at 2D wing section	β	Angle between skin-friction lines and boundary-layer edge flow, [deg]
c	Wing chord, [m]	β	Constant in the Lamb-Oseen vortex model, $\beta = 1.25643$
c_p	Pressure coefficient, $c_p = \frac{p - p_\infty}{q_\infty}$	Γ	Circulation, [m ² /s]
G	Relative circulation, $G = \Gamma/\Gamma_0$	Γ_0	Root circulation, [m ² /s]
g	Prism Layer Stretching Factor	δ	Wake edges
h_1	Initial Prism Layer Thickness, [m]	ε	Vortex-line angle, [deg]
L	Lift, [N]	ζ	Dimensionless axial vorticity ($\omega(b/2)/U_\infty$)
l_μ	Mean aerodynamic chord, [m]	Λ	Wing aspect ratio
Ma	Mach number	λ	Wing taper ratio
p	Static pressure, [N/m ²]	ρ_∞	Free stream density, [kg/m ³]
p_∞	Free stream static pressure, [N/m ²]	σ	Dimensionless circulation $\Gamma/(U_\infty(b/2))$
q_∞	Free stream dynamic pressure, [N/m ²], $q_\infty = \frac{\rho_\infty \cdot U_\infty^2}{2}$	τ^*	Dimensionless time ($x^* 16c_L)/(\pi^4 \Lambda)$
r	Radius, [m]	φ_{25}	Wing sweep related to the quarter line, [deg]
r_c	Vortex radius, [m]	Ψ	Flow shear angle, [deg]
Re	Reynolds number	Ω	Local vorticity content, [m ² /s ²]
T_∞	Reference temperature, [K]	ω	Vorticity, [1/s]
t	Physical time, [s]	<i>Subscripts</i>	
U_∞	Free stream velocity, [m/s]	l	Lower
V_θ	Circumferential velocity, [m/s]	u	Upper
v^1, v^2, v^3	Velocities in the local wake coordinate system, [m/s]	e	External inviscid flow
x, y, z	Cartesian coordinates, [m]		
x^*, y^*, z^*	Dimensionless coordinates		

1 INTRODUCTION

In this paper the vortex sheet and trailing vortex of a generic transport-aircraft configuration are investigated. The analysed geometry is the Common Research Model (CRM), which was also used for the fifth AIAA CFD Drag Prediction Workshop [1]. The numerical investigations are undertaken with a hybrid RANS solver, the DLR TAU-Code, which was developed by the German Aerospace Center (Deutsches Zentrum für Luft- und Raumfahrt, DLR) Institute of Aerodynamics and Flow Technology. The objectives are to investigate the trailing-edge flow and to validate the trailing-edge compatibility condition. Furthermore, the roll-up process of the vortex sheet within the wake is illustrated and several properties of the wake-vortex system are analysed with respect to their development in downstream direction.

The Common Research Model

The CRM is a wing/body/nacelle/pylon/horizontal-tail configuration with supercritical wing design. The development of the CRM was motivated by the demand for a contemporary experimental database by different parties [2]. The CRM is a low-wing configuration optionally provided with nacelle and pylon and/or horizontal tail. It is based on a transonic transport-aircraft configuration with a design cruise Mach number of $Ma = 0.85$ and a design lift coefficient $c_L = 0.5$ at a Reynolds number of $Re = 40 \cdot 10^6$ based on the mean aerodynamic chord l_μ . It features an aspect-ratio of $\Lambda = 9$, a taper-ratio of $\lambda = 0.275$ and a wing sweep related to the quarter line of $\varphi_{25} = 35.0^\circ$. With these basic guidelines in mind a wing geometry was derived. The reference quantities are summarised in Table 1. Note that A_{ref} is the Wimpres area introduced by Boeing, which differs from the definition of the reference area usually used at Airbus. The wing airfoils were constructed to be suitable not only for the design cruise conditions but for a small range around it. The outboard wing carries supercritical airfoil sections with a camber of about 1.5% and the wing trailing edge features a constant thickness of $3.556 \cdot 10^{-4} m$. Figure 1 shows the CRM planform and some of its dimensions. The position of the Yehudi break is at 37% wing half span. The designed airfoil sections and twist of the wing correspond to a nominal 1-g wing at cruise. The horizontal tailplane was designed with a symmetric airfoil and has a trapezoidal planform. The investigations presented in this paper are undertaken on the Wing/Body/Tail configuration with a horizontal-tail installation angle of zero degree, see Figure 2.

A_{ref}	$383.69 m^2$	λ	0.275
l_μ	$7.00532 m$	φ_{25}	35.0°
b	$58.763 m$	Λ	9

Table 1: CRM reference quantities.

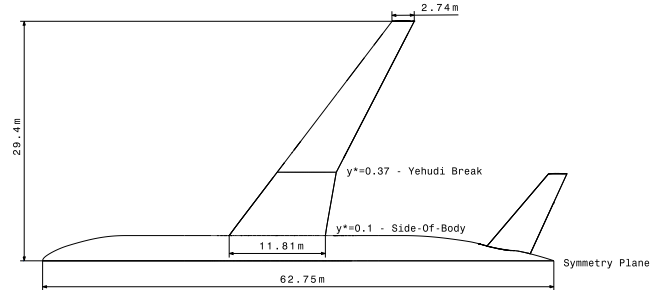


Figure 1: Planform of the CRM.

2 THE TRAILING-EDGE COMPATIBILITY CONDITION

This section describes the flow situation at the wing trailing edge and how local features of the wake near the trailing edge can be related to the spanwise distribution of the circulation at the lifting wing. For a valid mathematical description of a real flow at a lifting wing, the vortex layer formed in the wake must be taken into account. Figure 3a illustrates an idealised three-dimensional wake of the viscous flow around a lifting wing in subcritical motion. The flow can be divided into two counterparts, the viscous part near the wing surface, marked by reduced velocity, and the inviscid external flow. The viscous part is influenced by the boundary layer of the airfoil and carries the friction and pressure drag. $\vec{v}_{e,u}$ and $\vec{v}_{e,l}$ are the velocities at the upper edge δu and the lower edge δl of the wake, respectively. The velocities are defined as

$$(1) \quad \vec{v}_e = [v_e^1, v_e^2, v_e^3]^T.$$

The superscripts denote the directions in the local wake coordinate system. In the two-dimensional case the x^1 -

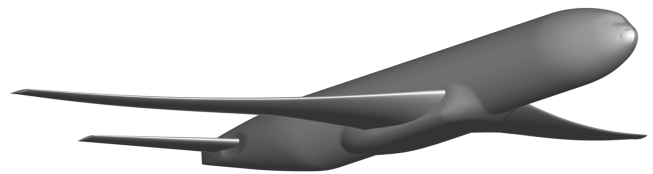


Figure 2: The Common Research Model (CRM).

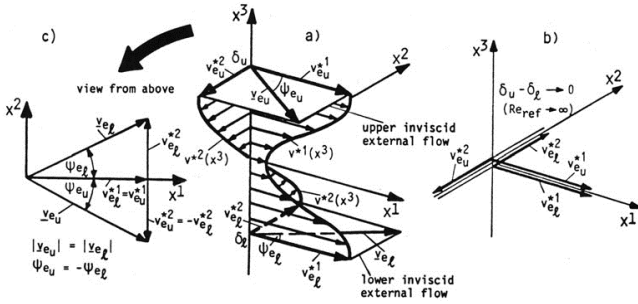


Figure 3: Three-dimensional idealised wake of a lifting wing in steady subcritical motion (right hand side of wing). a) idealised wake in reality, b) wake in the limit of $Re_{ref} \rightarrow \infty$, c) local wake coordinate system [3].

direction is aligned along the freestream direction. The x^2 -direction is aligned in crossflow direction. Because $|\vec{v}_{e,u}| = |\vec{v}_{e,l}|$ holds for the subcritical case, the x^1 -direction can be defined as the bisector of the upper and lower inviscid external velocity vectors, see Figure 3 c). The shear angle Ψ_e is defined as the angle between the x^1 -direction and the inviscid external velocity vectors. Based on this definition of the local wake coordinate system, the velocity profile can be divided into its x^1 - and x^2 -direction as it is seen in 3 a). The observed crossflow velocities in x^2 -direction represent the sheared flow at the upper and lower side of the lifting wing. The pressure compensation between the upper and lower side of the wing induces a crossflow velocity towards the wing tip at the lower side and towards the wing root at the upper side. Subsequent statements can be made for the quantities given in Figure 3 a,c):

$$(2) \quad \begin{aligned} |\vec{v}_{e,u}| &= |\vec{v}_{e,l}| \\ v_{e,u}^1 &= v_{e,l}^1 \\ v_{e,u}^2 &= -v_{e,l}^2 \\ \Psi_{e,u} &= -\Psi_{e,l} \end{aligned}$$

Applying the limiting process $Re \rightarrow \infty$, the thickness of the wake tends to zero and a discontinuity layer is formed, see Figure 3b). Concerning this limiting process, it can be shown that the flow modelled by the Navier-Stokes equations leads from the boundary layer description to the potential flow model. The local vorticity content introduced in [4] can be used for this purpose. According to Refs. [3, 5] the local vorticity content Ω of a shear layer is given as

$$(3) \quad \vec{\Omega} = [\Omega^1, \Omega^2, \Omega^3]^T = \int_{\delta_l}^{\delta_u} \vec{\omega} dx^3$$

with the vorticity vector $\vec{\omega}$. Only the boundary-layer terms are kept for the vorticity vector and thus reads

$$(4) \quad \vec{\omega} = [\omega^1, \omega^2, \omega^3]^T = \left[-\frac{\partial v^2}{\partial x^3}, \frac{\partial v^1}{\partial x^3}, 0 \right]^T.$$

According to Refs. [4] and [6], the vorticity content for a subcritical three-dimensional case can be written as

$$(5) \quad \vec{\Omega} = [v_{e,u}^2 - v_{e,l}^2, 0, 0]^T = [2v_{e,l}^2, 0, 0]^T.$$

The local vorticity content can be expressed via the shear angle Ψ as

$$(6) \quad \vec{\Omega} = [-2|\vec{v}_{e,l}|\sin\Psi_{e,l}, 0, 0]$$

with the shear angle

$$(7) \quad \sin\Psi_{e,l} = -\sin\Psi_{e,u} = \frac{v_{e,l}^2}{|\vec{v}_{e,l}|}.$$

As it is described in Ref. [7], a relation between the shear angle Ψ_e and the circulation along the wing can be made. The local vorticity content of the wake represents a flux of longitudinal vorticity away from the trailing edge. The change of the circulation in spanwise direction of the wing must be equal to that flux.

$$(8) \quad \Omega^1 = -2|\vec{v}_{e,l}|\sin\Psi_{e,l} = \frac{d\Gamma}{dy}$$

A more detailed description of the derivation of the local vorticity content is available in [4] and [8]. Note that Equation 8 is not strictly valid for the investigated case, because the limitation process $Re_{ref} \rightarrow \infty$ was necessary for the derivation of the equation [7].

Finally, the vortex-line angle ε is introduced, see Figure 4. If a forward or backward swept wing is considered, the x^1 -direction of the local wake coordinate system is not aligned along the freestream direction but slightly rotated about the vertical axis. The angle between the x -direction along the freestream velocity and the x^1 -direction of the local wake coordinate system is denoted as vortex-line angle ε . For backward swept wings the vortex-line angle is $\varepsilon > 0^\circ$ [5].

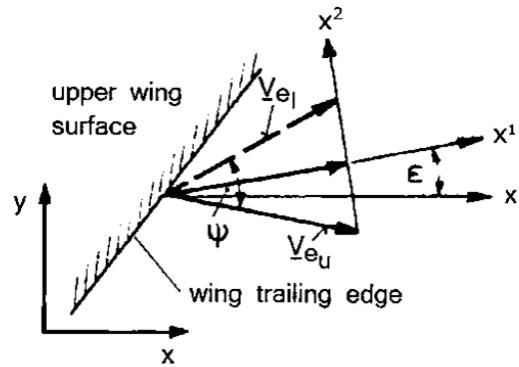


Figure 4: Flow situation at the wing trailing edge for a positively swept leading edge with the vortex-line angle ε [6].

3 NUMERICAL APPROACH

3.1 Grid Generation

The simulations are conducted on hybrid unstructured grids that are generated by means of the grid generation tool Centaur¹. Due to a symmetric model and symmetric freestream conditions it is possible to consider a half model. The created hybrid unstructured grid consists of an unstructured triangular surface grid, a prism layer covering the boundary-layer flow and tetrahedral elements within the remaining domain. The half model is embedded in a half sphere with a radius of $r = 100 \cdot l_{\mu}$ and a symmetry boundary condition at the symmetry plane. The surface elements are locally refined at the wing leading and trailing edge, the wing tip and the wing-body junction. Same holds for the horizontal tail. The prism layer is built by a wall normal extrusion of the surface elements. In order to properly resolve the boundary-layer flow a first cell height of $h_1 \approx 2.5 \cdot 10^{-5} m$ is applied. This results in a dimensionless wall distance of $y^+ \approx 0.67$. The first two prism layers are held at constant height and the remaining 31 prism layers feature a stretching factor of $g = 1.2$. The remaining domain is discretized by tetrahedral elements. In order to improve the quality of the numerical results, the triangular surface elements at the wing upper and lower side as well as at the wing trailing edge are replaced by quadrilateral elements, see Figure 5a. Structured hexahedral grid blocks can be attached to the resulting structured boundary-layer grid. Thus the wake-vortex system is meshed by structured hexahedral elements as well, see Figure 5b. The wake is resolved by the structured grid up to approximately 10 wing spans in downstream direction. The overall grid features $45 \cdot 10^6$ grid nodes and $114 \cdot 10^6$ grid elements.

3.2 Flow Solver

The applied flow solver is the DLR TAU-Code. It is a hybrid RANS solver developed by the German Aerospace Center (Deutsches Zentrum für Luft- und Raumfahrt, DLR) Institute of Aerodynamics and Flow Technology. The DLR TAU-Code solves the Reynolds-Averaged Navier-Stokes equations on hybrid grids. The solver is built from different modules, which can be executed independently. Two important modules are the preprocessor and the solver, cf. Ref. [9].

The preprocessor computes the dual grid data based on the primary grid cells. Therefore, the input for the preprocessing module is the primary grid and out of the primary grid the secondary grid is derived. Due to an edge-based data structure of the secondary grid, the primary grid can be built

¹CentaurSoft homepage: www.centaursoft.com. Last accessed on 25.10.2015.

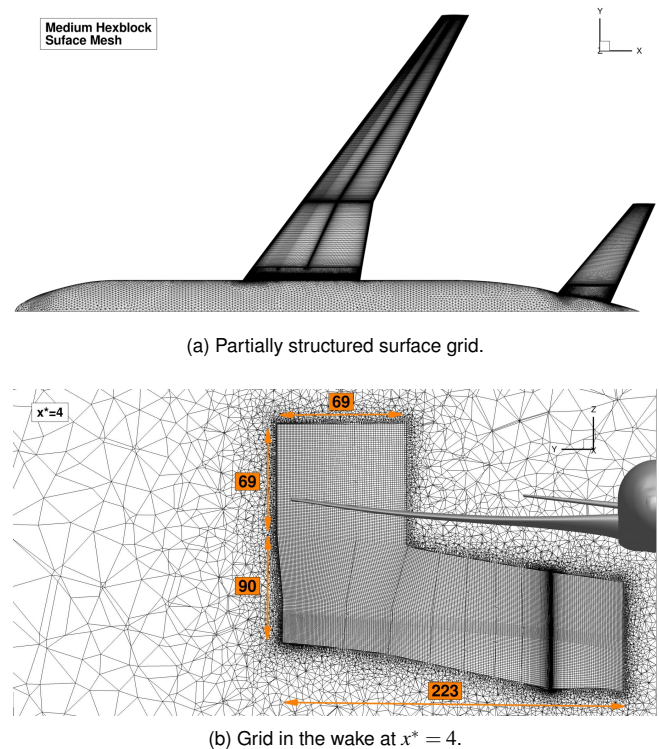


Figure 5: Partially structured grid of the CRM.

form arbitrary element types. Two different grid metrics are available, namely the cell vertex and the cell centered grid metric. The preprocessor also creates the additional grid(s), which is/are necessary for the multigrid approach.

The solver applies a finite volume scheme for solving the (unsteady) Reynolds-Averaged Navier-Stokes ((U)RANS) equations on the grid provided by the preprocessing module. Different methods are available for the spatial discretisation of the flow problem. The viscous and inviscid fluxes can be computed using either an upwind or a central scheme. Regarding temporal discretisation, different approaches (local, dual, global time stepping) are implemented, which provides the possibility of steady and time-accurate simulations. Different explicit and implicit algorithms are implemented for this purpose. Additional to the multigrid approach, a local time stepping concept and different residual smoothing algorithms are implemented for acceleration purposes [10].

3.3 Numerical Setup and Test Conditions

The performed simulations are based on a dual grid approach with a cell-vertex grid metric. The spatial discretisation is realised by a second-order central scheme introduced by Jameson [11]. A matrix dissipation scheme is used for artificial dissipation. The turbulent convective fluxes are discretised by a second-order upwind scheme.

The temporal discretisation is done by an implicit Backward-Euler scheme. The applied version uses a LU-SGS algorithm [12]. The unsteady simulations using the dual time approach are performed with a physical timestep of $\Delta t = 4.6 \cdot 10^{-4} s$. 150 inner iterations are conducted for each timestep. In order to accelerate the convergence of the solution, a 3v-multigrid cycle is used [13]. Turbulence modeling is realised by means of the Menter-SST eddy-viscosity turbulence model. The Schwarz limitation and the Positivity scheme are applied to increase stability [14]. The analysis is performed for one target flow condition with a Mach number of $Ma_\infty = 0.85$, a Reynolds number of $Re = 5 \cdot 10^6$, based on the mean aerodynamic chord l_μ , and an angle of attack of $\alpha = 2^\circ$. The reference temperature of $T_\infty = 310.93 K$ results in a freestream velocity of $U_\infty = 300.48 m/s$. The Reynolds number is chosen in accordance with former experimental investigations at the NASA Langley National Transonic Facility by Rivers and Dittberner [15]. The experimental results are used in order to evaluate the numerical results by means of surface pressure distributions, cf. Ref. [16]. The resulting flight condition features a lift coefficient of $c_L = 0.43$.

4 RESULTS AND DISCUSSION

4.1 Flow Past the Wing

The main focus of the analysis is the evaluation of the trailing-edge compatibility condition. Since the deflection of the wall-near flow at the wing trailing edge strongly depends on the present flow phenomena upstream of the trailing edge, the occurring effects are shortly described. Figure 6 summarises the present effects by means of skin-friction lines and surface pressure distribution. At the wing upper surface a shock can be observed, which is not strong enough to entail flow separation. However, the shock causes a deflection of the wall-near flow in direction of the

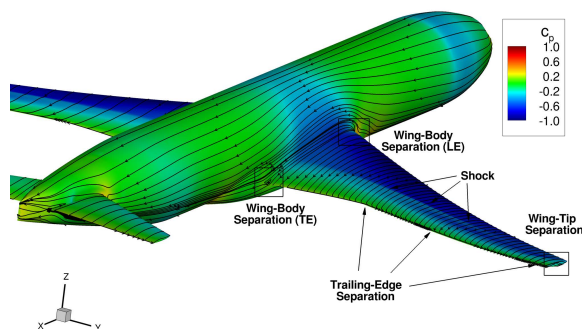


Figure 6: Overview of the occurring surface effects at the wing.

wing tip. Figure 7 illustrates the skin-friction lines (black) and the streamlines at the boundary-layer edge (red). β denotes the angle between the skin-friction lines and the boundary-layer edge flow. The shock significantly deflects the skin-friction lines towards the wing tip. However, the boundary-layer edge flow is not affected. This is indicated by the streamline patterns and the local peak of β . Consequently, the trailing-edge compatibility condition, which is evaluated at the boundary-layer edge, is assumed to be valid despite the present shock. At the wing trailing edge a separation takes place in the area of $0.37 \leq y^* \leq 0.9$, which starts at approximately 98% of the local chord length. The skin-friction line deflection is significant since they are aligned parallel to the trailing edge in this area. The considerably increased β -values near the trailing edge in Figure 7 indicate a large deviation between the skin-friction lines and the boundary-layer edge flow, which is additionally seen by the streamline patterns. It can be observed, that the boundary-layer edge flow is not considerably influenced by the trailing-edge separation. As a consequence, the trailing-edge compatibility condition is assumed to be applicable despite the trailing-edge separation.

Two different effects are observed at the wing-body junction. In the area of the wing leading edge a horse-shoe vortex is present. The skin-friction patterns in Figure 8a show a primary and a secondary vortex. They are indicated by the marked separation and attachment points and lines. The secondary separation and attachment lines indicate the presence of a secondary vortex. As the horse-shoe vortex moves away from the wing surface, it has no significant influence on the trailing-edge flow. At the wing trailing edge, a separation can be observed at the upper side of the wing in the region of the wing-body junction. Wing-body configurations generally feature a flow separation at certain angles of attack at a similar location [17]. During the 4th

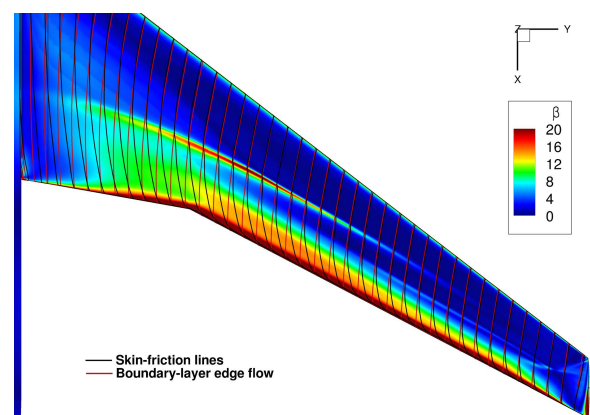
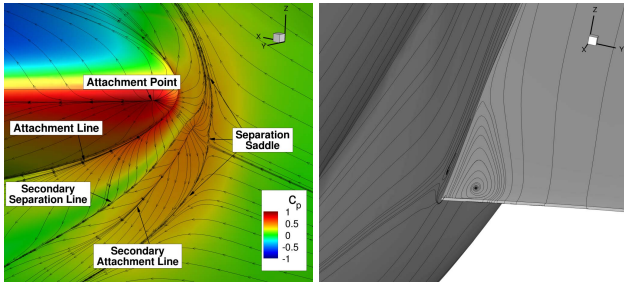


Figure 7: Skin-friction patterns (black), inviscid external streamlines (red) and angle β between both at the wing upper side.



(a) Wing-body leading-edge inter-section. (b) Wing-body trailing-edge separation.

Figure 8: Skin-friction patterns of the wing-body separations.

AIAA Drag Prediction Workshop several participants found the same separation at a slightly higher angle of attack [18]. Although the separation is present for different numerical results, it could not have been confirmed by experimental data yet [19]. Subsequent analyses on the trailing-edge flow reveal, that the flow separation at this location is distinct enough in order to distort the results of the compatibility condition.

Due to the flow around the wing tip, flow separation occurs at the upper side of the wing tip. The separated flow rolls up to a discrete vortex, which merges in the wake with the rolling up vortex layer. Due to the strength of the vortex it exhibits a primary, secondary and tertiary vortex structure. However, since the evolving tip vortex is limited to the wing-tip area, the influence on the trailing-edge compatibility condition is small and can be neglected.

4.2 Trailing-Edge Compatibility Condition

The trailing-edge compatibility condition is evaluated shortly behind the wing trailing edge by means of the wake profiles over the wing half span. Figure 9 exemplarily presents the dimensionless velocities v^1/U_∞ and v^2/U_∞ as well as the dimensionless axial vorticity $\zeta = \omega(b/2)/U_\infty$ as function of $z^* = z/(b/2)$, at $y^* = y/(b/2) = 0.6$ and $x/c = 1.03$, in the local wake coordinate system. The edges of the wake are determined by means of the axial vorticity at $\omega(y^*, z^*)/\omega_{max}(y^*) = 0.01$. This is a suitable approach since axial vorticity is only present in the vortex layer and the trailing vortex of the wake. The edges of the vortex layer are highlighted by the dashed lines. The wake edges are at $z^* \approx |0.005|$ at the considered lateral position. The dip in the axial velocity represents the boundary-layer flow floating-off the wing. The axial velocity significantly changes inside the wake. Outside the wake, the changes with respect to the vertical axis are very small. Regarding the lateral velocity profile, the influence of the trailing-edge separation on

the boundary-layer flow is clearly noticed. However, outside the wake the changes with respect to the vertical axis are very small. This indicates that the trailing-edge separation has no significant influence on the boundary-layer edge flow. The lateral shear of the trailing-edge flow is clearly observed by the different lateral velocity values at the upper and lower wake edge. In order to evaluate the trailing-edge compatibility condition the velocities and the local flow shear angle are determined at the wake edges. The evaluation is conducted at $x/c = 1.005$ as function of the wing half span. The obtained results are summarised in Figure 10. The necessary quantities are plotted versus the dimensionless wing half span y^* . In Figure 10a the dimensionless wake thickness z^* is illustrated. The black line represents the upper edge and the blue line the lower edge of the wake. The wake becomes thicker towards the wing root, which is reasonable since the wing chord gets longer and thus the boundary-layer thickness grows over a larger distance. Furthermore, the upper side of the wake is thicker, because of the stronger adverse pressure gradient compared to the lower side of the wing. Figure 10b shows the lateral velocity components at the wake edges in the local coordinate system. Due to the definition of the local coordinate system, the velocities at the wake edges are symmetric to the $v_e^2 = 0$ axis. The expected deflection of the flow towards the wing root on the upper side of the wing and towards the wing tip on the lower side of the wing is observed. The high velocity magnitudes at the wing tip considerably decrease towards the wing root within the region of $0.8 \leq y^* \leq 1$. At $y^* = 0.37$ a small peak is visible, which results from the Yehudi break. It represents a kink in the trailing edge of the wing. An illustration of the Yehudi break is given in Figure 1. Inboard of the Yehudi break the velocity magnitude further decreases and passes the zero velocity at $y^* \approx 0.2$. This effect is caused by the trailing-edge separation at the wing-body junction, which is not covered by the applied compatibility condition. However, this effect is only present at the very inboard section, which does not influence the trailing-edge compatibility condition further outboard. Figure 10c depicts the flow-shear angle Ψ and the vortex-line angle ε . The vortex-line angle is positive yielding values of about $\varepsilon \approx 2^\circ$, which confirms the expectations for configurations with backward-swept wings. Since the flow-shear angle Ψ is obtained by the velocity components, the distribution is comparable to the one presented in Figure 10b. The flow-shear angle Ψ significantly increases towards the wing tip and exhibits a small peak at the Yehudi break. Due to the change of the lateral velocity direction near the wing root, the flow-shear angle reveals a change of its sign at the same location as well. The flow-shear angle Ψ and the velocity components at the wake edges v_e are exploited in order to determine the local vorticity content Ω^1 , illustrated in

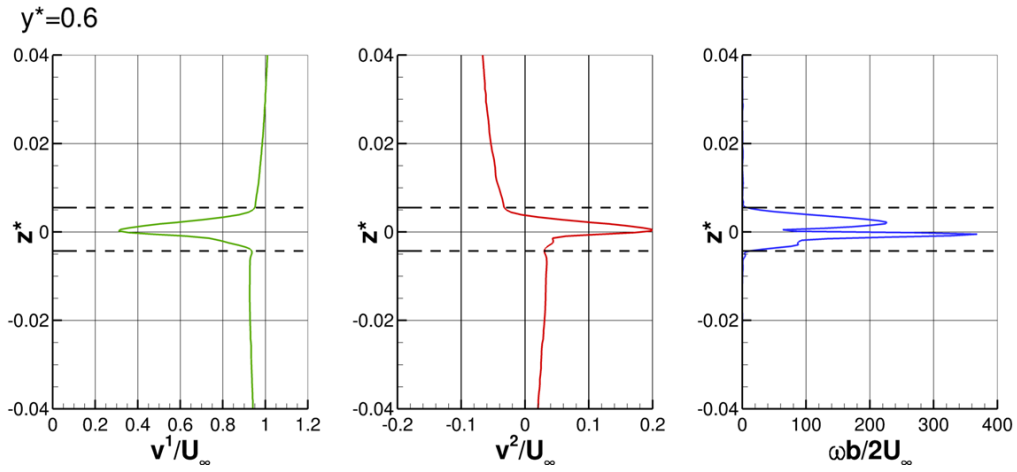
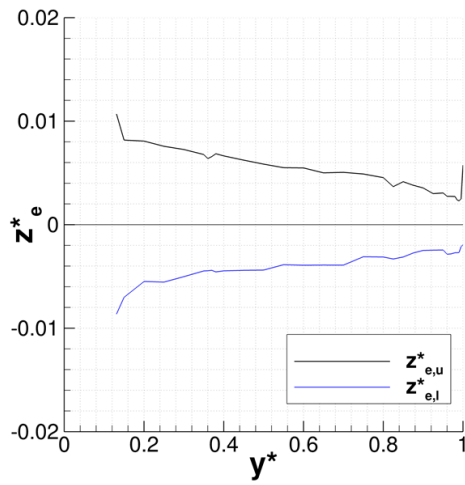
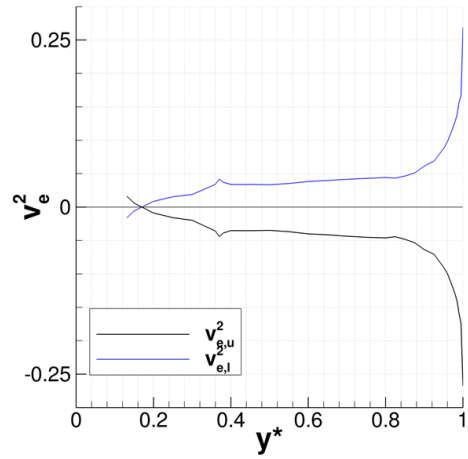


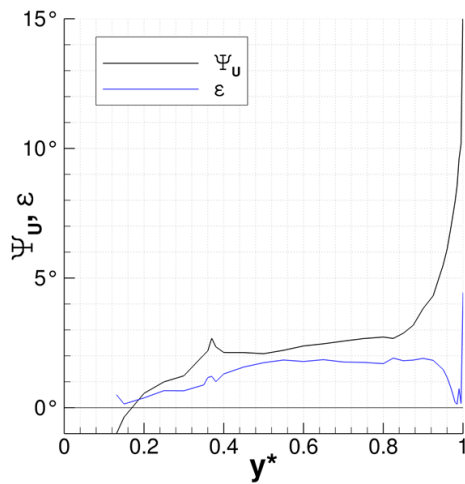
Figure 9: Wake profiles at $y^* = 0.6$ and $x/c = 1.03$.



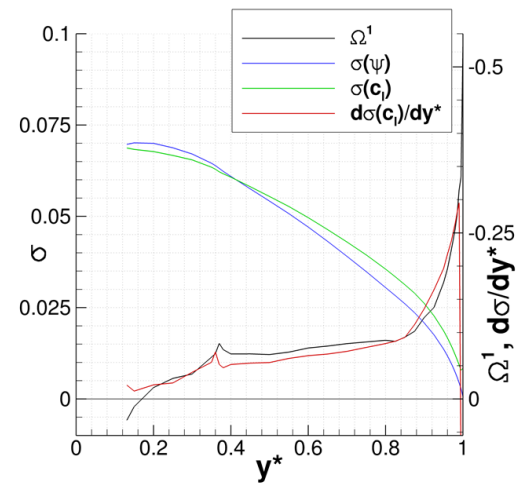
(a) Wake thickness as function of the wing half span.



(b) Lateral velocity as function of the wing half span.



(c) Shear angle and vortex line angle as function of the wing half span.



(d) The local vorticity content, the dimensionless circulation obtained by the trailing-edge compatibility condition $\sigma(\Psi)$ and the Kutta-Joukowski theorem $\sigma(c_t)$ and its spanwise derivative.

Figure 10: Evaluation of the trailing-edge compatibility condition at $x/c = 1.005$.

Figure 10d (black). Since the local vorticity content equals the spanwise derivative of the circulation $d\Gamma/dy^*$, the integral represents the spanwise circulation distribution $\Gamma(y^*)$. In the analysis exclusively the dimensionless formulation of the circulation $\sigma = \Gamma/(U_\infty(b/2))$ is applied. The dimensionless circulation $\sigma(\Psi)$ is highlighted by the blue line in Figure 10d. A typical distribution including a strong increase near the wing tip and reaching a maximum towards the wing root can be observed. Due to the disturbance of the flow at the trailing edge in the region of the wing root, the circulation slightly decreases in this area. Therefore, the root circulation does not yield the maximum circulation of the spanwise distribution. In order to validate the trailing-edge compatibility condition, the circulation is additionally determined by means of the Kutta-Jukowski theorem. The dimensionless circulation distribution obtained by the Kutta-Jukowski theorem $\sigma(c_l)$ is illustrated in green. It shows a comparable distribution to the integral values of the local vorticity content. In the outboard wing section the Kutta-Jukowski theorem predicts slightly larger circulation values and inboard of the Yehudi break it predicts slightly reduced values in comparison with the results obtained by the compatibility condition. Concerning the root circulation of both approaches, similar values are obtained ($\sigma_0(\Psi) = 0.0697$ and $\sigma_0(c_l) = 0.068$). The spanwise derivative of $\sigma(c_l)$ represents the deviations observed in the circulation distribution. However, the characteristics of the local vorticity content and the circulation derivative are quite similar. Both predict high values in the outboard section and account for the influence of the Yehudi break. Nevertheless, the absolute values slightly differ. The area near the root chord reveals significant deviations since the trailing-edge compatibility condition is not able to cope with such distinct flow separations. However, the conducted analysis confirms the applicability of the presented trailing-edge compatibility condition, although the investigated case

features a discontinuity (shock), a varying trailing-edge contour (Yehudi break), small scale flow separation (trailing-edge separation) and viscous flow.

4.3 Wake-Vortex System

The wake-vortex system of the considered transport-aircraft configuration consists of a wing vortex layer rolling-up to the trailing vortex and the rolling-up vortex layer of the horizontal tail. The tip vortex of the wing merges with the rolling-up trailing vortex immediately behind the trailing edge. An overview of the wake-vortex system is given in Figure 11. The vortex layers and trailing vortices are visualised by the axial vorticity. Considering the starboard side, the vortex layer and trailing vortex of the lifting wing feature positive values, which indicates a clockwise rotation. The vortex layer of the horizontal tail, however, indicates a counter-clockwise rotation by negative values on the same side. Consequently, a negative lift coefficient results for the horizontal tail, which is caused by the induced downwash in the wake of the lifting wing. The vortex core of the trailing vortex exhibits significantly increased axial vorticity values compared to the vortex layer. In downstream direction, the trailing vortex increases in size and the axial vorticity simultaneously decreases. The whole wake-vortex system sinks in downstream direction, whereas the downward motion of the vortex layer is more distinct at the inboard section. At the very inboard area of the wake, an interaction of the wing vortex layer and the horizontal-tail vortex layer is observed. Both vortex layers start to rotate around each other and the wing vortex layer is split into two separate parts. It can be seen that the roll-up process is not finished at the end of the resolved numerical grid at $x^* = 10$. A detailed presentation of the wake-vortex system is given in the appendix in Figure 15.

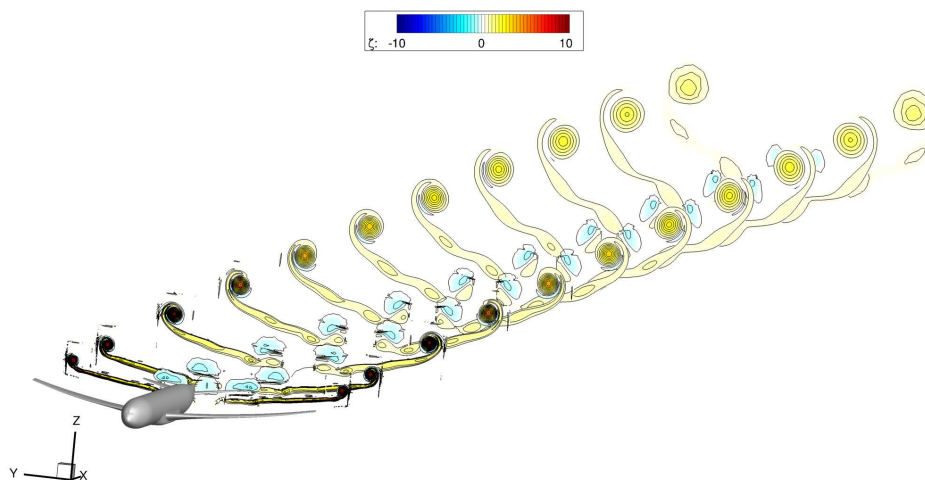


Figure 11: Wake-vortex system visualised with the non-dimensional axial vorticity.

If inviscid flow is assumed, the vorticity, which is in the vortex layer and the trailing vortex, equals the root circulation and is constant in downstream direction. Only the distribution of the vorticity between the vortex layer and the trailing vortex changes since the vortex layer rolls-up with the trailing vortex. If the roll-up process is finished, a discrete vortex with a circulation of Γ_0 for each wing half is left. Although the investigated case considers viscous flow, the summarized circulation in the wake near the trailing edge must approximately equal the root circulation at the wing. The development of the circulation in downstream direction gives information about the grid resolution, since a significantly decreasing circulation would indicate strong numerical dissipation. Figure 12 presents the relative circulation $G = \Gamma(x^*)/\Gamma_0$ in the wake region. The circulation is calculated by means of a surface integral of the axial vorticity in several survey planes with $x^* = const.$ for each plane. The black line indicates the distribution including the negative part of the horizontal-tail vortex layer. The blue line represents the distribution of the wing vortex layer exclusively. The value of approximately one indicates the equality of the bound circulation at the wing and the circulation in the wake-vortex system. Furthermore, the circulation reveals an almost constant distribution in downstream direction up to $x^* = 9$. This indicates a good grid resolution and small numerical dissipation, since slight dissipation is caused by the viscous diffusion. Due to the fact that the fine grid resolution ends at $9 < x^* < 10$, the circulation significantly drops at $x^* = 10$.

Another interesting quantity is the circulation of the trailing vortex. The conservation of the circulation within the wake was already proven. According to the theory, the circulation of the trailing vortex should constantly increase within the considered wake region, because the roll-up process is not finished. The circulation of the vortex is determined via the circumferential velocity V_θ by $\Gamma(r) = 2\pi V_\theta(r)U_\infty$ and via

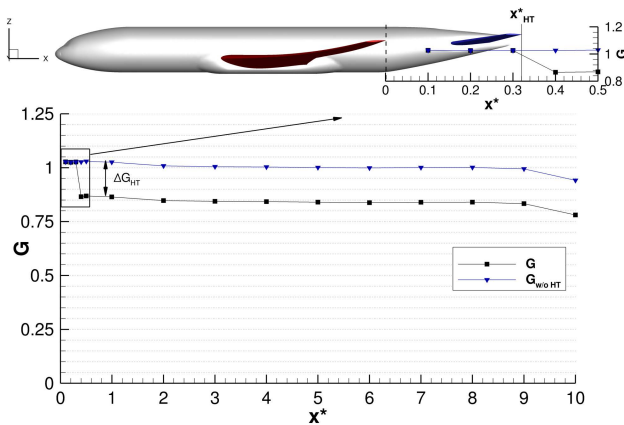


Figure 12: Distribution of the circulation in the wake region.

the axial vorticity ω_x by $\Gamma = \iint_{(F)} \omega \cdot dF$. The circulation of the trailing vortex via V_θ is calculated along the marked line in Figure 13a. In order to determine the circulation $G(\omega_x)$, the axial vorticity is integrated over the vortex area as it is marked in Figure 13c. Preliminary to the determination of the trailing vortex circulation by means of the circumferential velocity, the radial distribution of V_θ is checked, see Figure 13b. The circumferential velocity obtained by the numerical results is compared to the analytical solution of the Rankine vortex

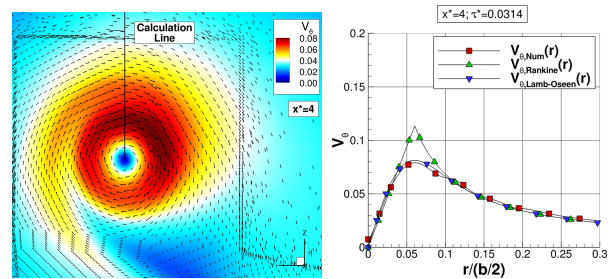
$$(9) \quad V_\theta = \begin{cases} \frac{\Gamma_0}{2\pi r_c} \frac{r}{r_c} & : r \leq r_c \\ \frac{\Gamma_0}{2\pi r} & : r > r_c \end{cases}$$

and the Lamb-Oseen vortex

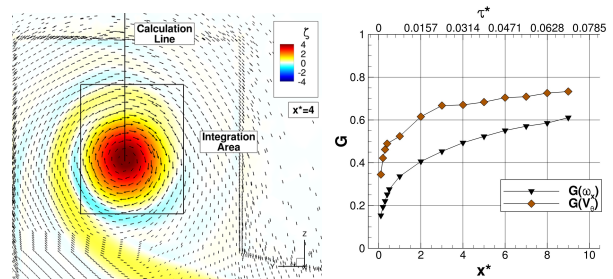
$$(10) \quad V_\theta = \frac{\Gamma_0}{2\pi r} \left[1 - e^{-\beta \left(\frac{r}{r_c}\right)^2} \right]$$

A detailed description of the analytical vortex models is given in Ref. [20]. The distributions of the velocities show good agreement over a wide range of the radius. The Rankine model can not represent the correct distribution at the viscous core of the vortex since no viscosity is considered. In contrast, the Lamb-Oseen model represents the velocity distribution very well.

The resulting circulations obtained by the two approaches are given in Figure 13d. The significant deviations can be



(a) Circumferential velocity and tangential vectors at $x^* = 4$. (b) Circumferential velocity as function of the radius in comparison with theoretical velocity distributions.



(c) Axial vorticity distribution and integration area at $x^* = 4$. (d) Circulation of the trailing vortex for two calculation methods as function of x^* .

Figure 13: Analysis of the trailing vortex.

explained by the asymmetrical velocity distribution of the trailing vortex. The marked line in Figure 13a utilized to calculate the circulation is located in an area of increased velocity. Consequently, the resulting circulation can not be correctly represented for the trailing vortex. The integral of the axial vorticity shows reduced values compared to the circulation obtained by V_θ . In addition to the asymmetric trailing vortex, the deviations can be associated to the chosen length of the integration line and the size and location of the integration area. Despite the deviations in the absolute values, both approaches predict the increase of the circulation within the trailing vortex. Although the growth rate steadily decreases, a significant increase is still present at $x^* = 9$.

Figure 14 illustrates the evolution of the wake-vortex system. The vortex layers and trailing vortices are visualised by means of the axial and lateral vorticity. The illustration represents the wake-vortex system 0.14 s after the beginning of the simulation. It can be observed that the starting vortices of the wing and the horizontal tailplane are floating off in downstream direction. The vortices indicate opposite rotation, which can be identified by the contour plots of the vorticity. This is a consequence of lift at the wing and downforce at the horizontal tail. The downforce at the horizontal tailplane is induced by the downwash in the wake of the lifting wing. In addition, the evolving roll-up process of the vortex layer and the merging of the tip vortex with the vortex layer can be seen.

5 CONCLUSION AND OUTLOOK

Numerical investigations on a generic transport-aircraft configuration, namely the NASA Common Research Model, have been conducted at cruise conditions. A hybrid unstructured numerical grid with partly structured grid areas has been applied. Unsteady RANS simulations have been

performed employing the DLR TAU-Code. The turbulence modelling has been realised by the two-equation eddy-viscosity Menter-SST model. The main focus of the investigations has been set on the trailing-edge flow and the development of the wake-vortex system. The trailing-edge flow has been investigated using velocity and vorticity profiles. Applying these flow properties, the trailing-edge compatibility condition has been evaluated. The compatibility condition gives a relation of local flow properties at the wing trailing edge and the bound circulation at the wing. Although the investigated case does not exactly meet the restrictions made in the derivation of the compatibility condition, the circulation distribution is well predicted by this condition. However, the trailing-edge compatibility condition can not cope with large scale flow separations. The wake-vortex system is resolved up to ten wing spans in downstream direction. The evolving rolling up of trailing vortex layer is visualised and the downward motion of the wake-vortex system is observed. The circulation of the wake-vortex system corresponding to the bound circulation at the wing and the circulation conservation in downstream direction are proven. Furthermore, some trailing-vortex properties like the circulation in the trailing vortex are analysed. Finally, the starting vortices of the wing and the horizontal tailplane are presented. The starting vortices and the evolving roll-up process of the vortex layer are well predicted by the numerical simulation. As a result, the trailing-edge compatibility condition is valid for this generic transport-aircraft configuration at cruise conditions. In a next step a more realistic configuration with attached nacelle and pylon could be investigated. Furthermore, the influence of a shock induced flow separation for slightly larger angles of attack could be analysed. In order to obtain an improved representation of the flow physics RSM models or DES investigations might be beneficial.

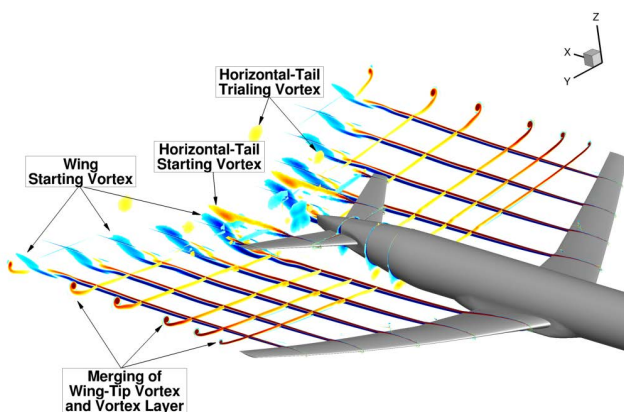


Figure 14: Starting Vortex.

ACKNOWLEDGEMENTS

The support of this investigation by Dr.-Ing. Andreas Hövelmann, Prof. Dr.-Ing. Christian Breitsamter and Prof. Dr.-Ing. Ernst-Heinrich Hirschel is gratefully acknowledged. Furthermore, the author thanks the German Aerospace Center (DLR) for providing the DLR TAU-Code used for the numerical investigations. The support of CENTAURSoft for its guidance during the mesh generation process is also highly appreciated. Moreover, the author gratefully acknowledges the Gauss Centre for Supercomputing e.V. (www.gauss-centre.eu) for funding this project by providing computing time on the GCS Supercomputer SuperMUC at Leibniz Supercomputing Centre (LRZ, www.lrz.de).

REFERENCES

- [1] Levy, D. W., Laflin, K. R., Tinoco, E. N., Vassberg, J. C., Mani, M., Rider, B., Rumsey, C. L., Wahls, R., Morrison, J. H., Brodersen, O., Crippa, S., Mavriplis, D. J., and Murayama, M., "Summary of Data from the Fifth Computational Fluid Dynamics Drag Prediction Workshop," *Journal of Aircraft*, Vol. 51, No. 4, 2014, pp. 1194–1213.
- [2] Vassberg, J. C., Dehaan, M., Rivers, M. B., and Wahls, R., "Development of a Common Research Model for Applied CFD Validation Studies," *26th AIAA Applied Aerodynamics Conference, Honolulu, Hawaii, No. 6919 in AIAA (2008)*.
- [3] Hirschel, E. H., "Vortex Flows: Some General Properties, and Modelling, Configurational and Manipulation Aspects," *14th AIAA Applied Aerodynamics Conference, New Orleans, United States, No. 2514 in AIAA (1996)*.
- [4] Hirschel, E. H. and Rizzi, A., "The Mechanism of Vorticity Creation in Euler Solutions for Lifting Wings," *Symposium on International Vortex Flow Experiment on Euler Code Validation*, edited by A. Elsenaar and G. Eriksson, FFA, Bromma, Sweden, 1986.
- [5] Hirschel, E. H. and Fornasier, L., "Flowfield and Vorticity Distribution Near Wing Trailing Edges," *22nd Aerospace Sciences Meeting, Reno, United States, No. 0421 in AIAA (1984)*.
- [6] Hirschel, E. H., Cousteix, J., and Kordulla, W., *Three-Dimensional Attached Viscous Flow: Basic Principles and Theoretical Foundations*, Springer Verlag, Berlin, Heidelberg, 2014.
- [7] Wanie, K. M., Hirschel, E. H., and Schmatz, M. A., "Analysis of Numerical Solutions for Three-Dimensional Lifting Wing Flows," *Zeitung für Flugwissenschaften und Weltraumforschung*, , No. 15, 1991, pp. 107–118.
- [8] Eberle, A., Rizzi, A., and Hirschel, E. H., *Numerical Solutions of the Euler Equations for Steady Flow Problems*, Vol. 34 of *Notes on numerical fluid mechanics*, Vieweg Verlag, Braunschweig, 1992.
- [9] Deutsches Zentrum für Luft- und Raumfahrt e.V. - Institute of Aerodynamics an Flow Technology, "Technical Documentation of the DLR TAU-Code Release 2014.2.0," 2014.
- [10] Gerhold, T., "Overview of the Hybrid RANS Code TAU," *MEGAFLOW - Numerical Flow Simulation for Aircraft Design*, edited by J. K. Fassbender and N. Kroll, Springer Verlag, 2005, pp. 81–92.
- [11] Jameson, A., Schmidt, W., and Turkel, E., "Numerical Solution of the Euler Equations by Finite Volume Methods Using Runge Kutta Time Stepping Schemes," *14th Fluid and Plasma Dynamics Conference, Palo Alto, United States, No. 1259 in AIAA (1981)*.
- [12] Jameson, A. and Yoon, S., "Lower-upper implicit schemes with multiple grids for the Euler equations," *AIAA Journal*, Vol. 25, No. 7, 1987, pp. 929–935.
- [13] Jameson, A. and Yoon, S., "Multigrid Solution of the Euler Equations Using Implicit Schemes," *23rd Aerospace Sciences Meeting, Reno, United States, No. 0293 in AIAA (1985)*.
- [14] Deutsches Zentrum für Luft- und Raumfahrt e.V. - Institute of Aerodynamics an Flow Technology, "TAU-Code User Guide Release 2015.1.0," 2015.
- [15] Rivers, M. B. and Dittberner, A., "Experimental Investigations of the NASA Common Research Model," *Journal of Aircraft*, Vol. 51, No. 4, 2014, pp. 1183–1193.
- [16] Pfnür, S., *Numerical Analysis of the Trailing-Edge Vortex Layer and the Wake-Vortex System of a Generic Transport-Aircraft Configuration*, Master's Thesis, Technische Universität München - Lehrstuhl für Aerodynamik und Strömungsmechanik, München, 2015.
- [17] Rossow, C. C., Wolf, K., and Horst, P., *Handbuch der Luftfahrzeugtechnik*, Carl Hanser Verlag GmbH & Company KG, 2014.
- [18] Brodersen, O., Crippa, S., Eisfeld, B., Keye, S., and Geisbauer, S., "DLR Results from the Fourth AIAA Computational Fluid Dynamics Drag Prediction Workshop," *Journal of Aircraft*, Vol. 51, No. 4, 2014, pp. 1135–1148.
- [19] Zilliac, G., Pulliam, T., Rivers, M. B., Zerr, J., Delgado, M., Halcomb, N., and Lee, H., "A Comparison of the Measured and Computed Skin Friction Distribution on the Common Research Model," *49th AIAA Aerospace Sciences Meeting including the New Horizons Forum and Aerospace Exposition, Orlando, United States, No. 1129 in AIAA (2011)*.
- [20] Breitsamter, C., *Nachlaufwirbelsysteme großer Transportflugzeuge: Experimentelle Charakterisierung und Beeinflussung*, Habilitation, Herbert Utz Verlag, München, 2007.

APPENDIX

A Wake-Vortex System

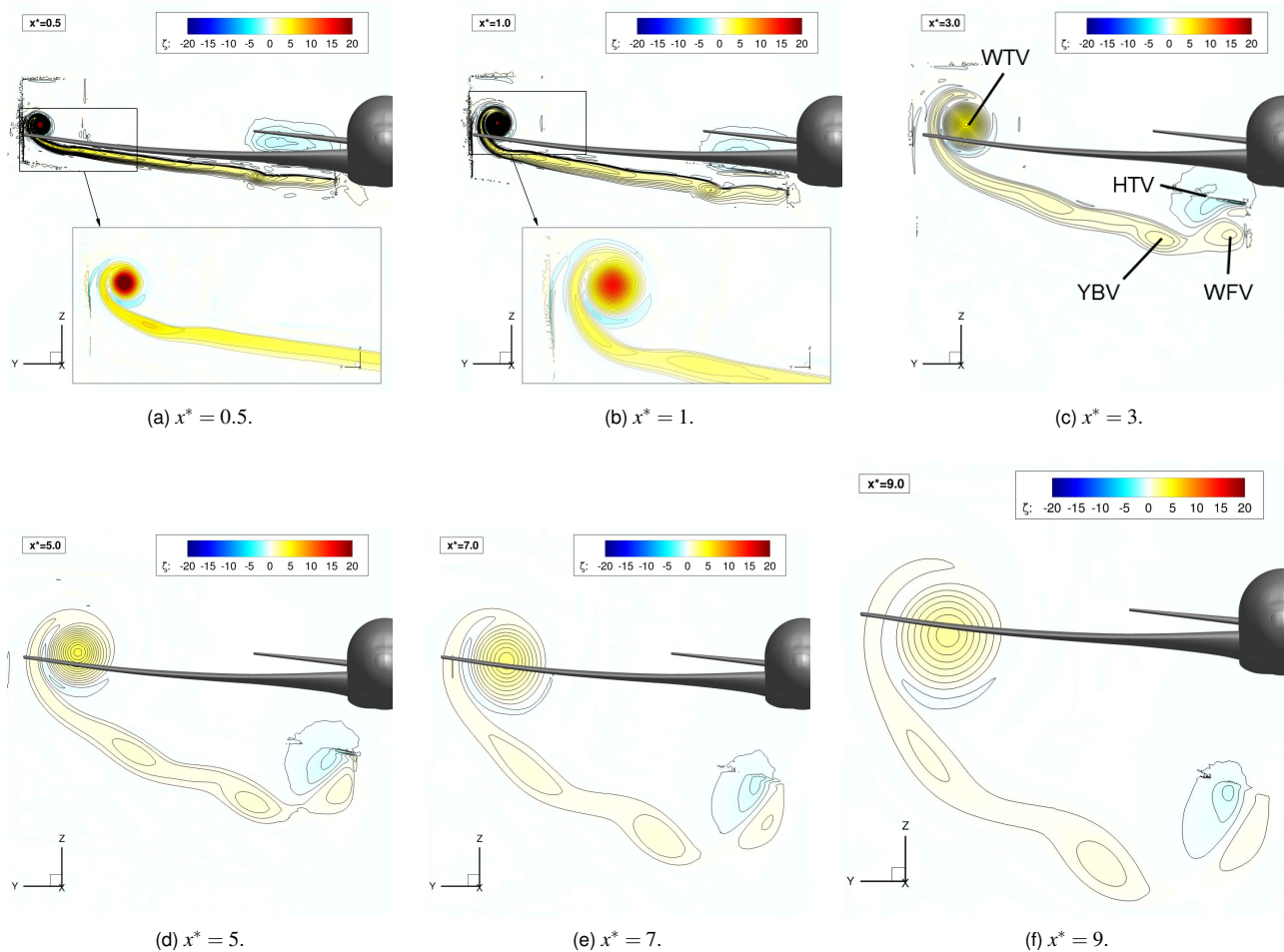


Figure 15: Development of the wake-vortex system visualised by the axial vorticity.

- WTV: Wing Tip Vortex
- WFV: Wing Fuselage Vortex
- YBV: Vortex due to kink in trailing edge
- HTV: Horizontal Tailplane Vortex